

# Quantum Dynamics in an Explicit Solvent Environment: A Photochemical Bond Cleavage Treated with a Combined QD/MD Approach

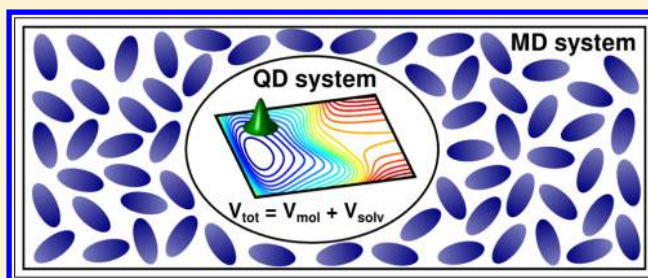
Sebastian Thallmair,<sup>†,‡</sup> Julius P. P. Zauleck,<sup>†</sup> and Regina de Vivie-Riedle<sup>\*,†</sup>

<sup>†</sup>Department Chemie, Ludwig-Maximilians-Universität München, D-81377 München, Germany

<sup>‡</sup>Lehrstuhl für BioMolekulare Optik, Ludwig-Maximilians-Universität München, D-80538 München, Germany

## S Supporting Information

**ABSTRACT:** In quantum chemistry methods to describe environmental effects on different levels of complexity are available in the common program packages. Electrostatic effects of a solvent for example can be included in an implicit or explicit way. For chemical reactions with large structural changes additional mechanical effects come into play. Their treatment within a quantum dynamical context is a major challenge, especially when excited states are involved. Recently, we introduced a method that realizes an implicit description. Here, we present an approach combining quantum dynamics and molecular dynamics. It explicitly incorporates the solvent environment, whereby the electrostatic as well as the dynamic effects are captured. This new method is demonstrated for the ultrafast photoinduced bond cleavage of diphenylmethylphosphonium ions ( $\text{Ph}_2\text{CH}-\text{PPh}_3^+$ ), a common precursor to generate reactive carbocations in solution.



## 1. INTRODUCTION

Solvents are an important aspect of every day chemistry.<sup>1</sup> While they are often only the reaction medium and do not participate directly in product formation, their electrostatic influence can stabilize or destabilize certain reaction pathways depending on the charge distribution along them.<sup>2,3</sup> In addition, dynamic effects of the solvent environment can emerge.<sup>4,5</sup> The solvent molecules directly interact with the molecular motion of the solute. In the case of ultrafast reactions like photochemical bond cleavage, where strong changes of the molecular structure occur, dynamic solvent effects are particularly important. The solute's fragments, moving apart, push into the solvent cage, and their initial motion is hindered. This can deviate their motion along a path less blocked by solvent molecules, and routes toward smaller energy gradients can come into play. In this way, the dynamics of the molecular system are substantially affected by the forces induced by the solvent cage and hence by its mechanical influence.

From a theoreticians point of view, the challenge is to treat the dynamic solvent effects during quantum dynamics (QD) simulations of photoinduced processes. A solution to treat this caging effect within the quantum mechanical framework in a continuum-like fashion was found recently.<sup>5</sup> The approach uses Stokes' law and the dynamic viscosity of the solvent to include the frictional force exerted on the molecular motion into the QD simulations. It was shown that the deceleration due to the environment is crucial for describing product formation during the bond cleavage of  $\text{Ph}_2\text{CH}-\text{PPh}_3^+$ . Another possibility for investigating the dynamic effect of the solvent environment is

to perform molecular dynamics (MD) simulations of the reactant in a box of solvent molecules. For photoinduced bond cleavage in ICN, parametrized potentials are available to simulate the excited state dynamics and to compare the gas phase with the behavior in different fluids, e.g., Xe,<sup>6</sup> Ar,<sup>7,8</sup> or  $\text{H}_2\text{O}$ .<sup>9</sup> Moskun et al. derived a microscopic picture of the rotational deceleration of  $\text{CN}^\bullet$  radicals after photochemical bond cleavage in liquid Ar by comparing classical MD simulations and transient pump–probe anisotropy measurements.<sup>10</sup>

Here, we present a new method that includes an explicit, atomistically modeled solvent environment in QD simulations on quantum chemical potential surfaces. The method is demonstrated for QD on a regular grid, which offers high flexibility in its applications. We use the photoinduced bond cleavage of  $\text{Ph}_2\text{CH}-\text{PPh}_3^+$  as an example. The selected solvent, acetonitrile (MeCN), does not react with the solute or its photoproducts. MD simulations are used to evaluate the solvent environment and to deduce the minimum number of coordinates required to describe the interaction between solvent and solute by means of a statistical analysis. The resulting solute solvent interaction energy is then calculated for each point of the ab initio potentials based on a quantum chemically precalculated database. Quantum dynamics are performed for many solvent arrangements, and their average leads to the overall picture of the bond cleavage.

Received: January 19, 2015

Published: March 20, 2015

This article is structured as follows: The description of our new QD/MD approach and the statistical rating of the coordinates for the solute solvent interaction are given in Section 2. This is followed by a brief summary of the computational details of the calculations (Section 3). The application of the QD/MD method to the photochemical bond cleavage of  $\text{Ph}_2\text{CH}-\text{PPh}_3^+$  and the discussion of the results are presented in Section 4.

## 2. INCLUDING THE EXPLICIT ENVIRONMENT INTO QUANTUM DYNAMICS

**2.1. Calculation of the Solvent Potential.** Our new QD/MD approach combines QD with an atomistic modeling of the solvent environment. The surrounding of the reactant enters the QD via an additional potential term  $\hat{V}_{\text{solv}}$  in the Hamiltonian, comparable to the dynamic continuum ansatz.<sup>5</sup>  $\hat{V}_{\text{solv}}$  contains the interaction energy between the reactant and its ambient solvent molecules. Thus, the Hamiltonian  $\hat{H}$  encompasses the operators for the kinetic energy of the nuclei ( $\hat{T}_{\text{nuc}}$ ), the molecular potential energy ( $\hat{V}_{\text{mol}}$ ), and the solvent potential ( $\hat{V}_{\text{solv}}$ )

$$\begin{aligned}\hat{H} &= \hat{T}_{\text{nuc}} + \hat{V}_{\text{mol}} + \hat{V}_{\text{solv}} \\ &= \hat{T}_{\text{nuc}} + \hat{V}_{\text{tot}}\end{aligned}\quad (1)$$

The sum of  $\hat{V}_{\text{mol}}$  and  $\hat{V}_{\text{solv}}$  is the total potential  $\hat{V}_{\text{tot}}$ . The time evolution of the wave function  $\Psi$  of the system is described by the time-dependent Schrödinger equation

$$i\hbar \frac{\partial}{\partial t} \Psi = (\hat{T}_{\text{nuc}} + \hat{V}_{\text{mol}} + \hat{V}_{\text{solv}}) \Psi \quad (2)$$

The solvent potential  $\hat{V}_{\text{solv}}$  is the sum of all individual interaction energies  $E_{\text{sf}}$  between the  $N_{\text{solv}}$  solvent molecules and the reactant described by the wave function  $\Psi$ . Consistent with a standard force field,  $\hat{V}_{\text{solv}}$  is described by two-body interactions. The reactant is partitioned into  $N_{\text{frag}}$  fragments, which, approximately, do not change their shape during the process. They are chosen to reflect the chemistry of the system, which means separation or reordering of the fragments model the major structural changes during the reaction. Each fragment contributes to  $\hat{V}_{\text{solv}}$

$$\hat{V}_{\text{solv}} = \sum_{i=1}^{N_{\text{solv}}} \sum_{j=1}^{N_{\text{frag}}} E_{\text{sf}}(q_1^{ij}, q_2^{ij}, q_3^{ij}, \dots, q_6^{ij}) \quad (3)$$

$E_{\text{sf}}$  depends on the relative orientation of the considered pair of solvent molecule  $i$  and fragment  $j$  and is a function of six degrees of freedom  $q_n^{ij}$  with  $n \in \{1, 2, \dots, 6\}$ , i.e., one distance and five angular coordinates (Figure 1). This is the number necessary to describe the relative orientation of two three-dimensional objects in a three-dimensional space. Each object requires three noncollinear rotational axes ( $R_{A1}$ ,  $R_{A2}$ ,  $R_{A3}$  and  $R_{B1}$ ,  $R_{B2}$ ,  $R_{B3}$ ) which can be chosen arbitrarily. If one axis of each object is collinear with the connecting vector between both centers of mass, which is the case for  $R_{A2}$  and  $R_{B2}$  in Figure 1, then one redundant degree of freedom can be removed. In addition, the distance between the centers of mass is necessary. Thus, altogether, six degrees of freedom fully describe the relative orientation of the solvent molecule  $i$  and the fragment  $j$  and constitute the orientation space.

The potential landscape for the arrangement of the solvent environment around a solute is very flat and has a large number

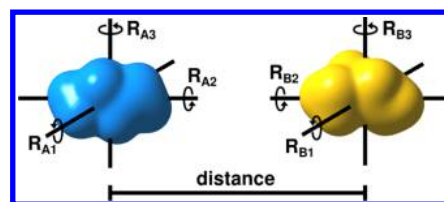


**Figure 1.** Illustration of the coordinates necessary to describe the relative orientation of two three-dimensional objects in three-dimensional space. One of the two rotational axis,  $R_{A2}$  and  $R_{B2}$ , can be left out if they are collinear with the connecting vector of both objects. Altogether, six degrees of freedom describe the relative orientation of both objects.

of energetically accessible regions around local minima at room temperature. This makes it nearly impossible to optimize a representative number of configurations around a medium-sized molecule. A convenient way to cover the thermodynamically accessible configuration space is to perform MD simulations of the reactant in a box of solvent molecules. From these, a sufficiently large number of snapshots along the trajectories represents the surrounding solvent. The MD simulations should be carried out for the reactant in its electronic ground state. This is also reasonable for the initial setting of the excited state dynamics, especially if ultrashort laser pulses are used for excitation. On this time scale, the nuclei of the solvent molecules cannot react to the electronic changes of the solute.<sup>11,12</sup> For each snapshot of the MD trajectories, the solvent potential  $V_{\text{solv}}$  has to be calculated, which is then used for a QD simulation. In addition, the QD simulations require the potential energy surfaces  $V_{\text{mol}}$  of the reactant, which are set up on a grid of selected coordinates. The Hamiltonian in eq 1 allows the setup in full dimensions; in our working example, we will follow the reaction in specially designed reactive coordinates  $\xi_i$ . For each grid point, the interaction energy  $E_{\text{sf}}$  between reactant and solvent molecules is evaluated in the six-dimensional orientation space by reading the current structure of the reactant and placing it at the respective position in the solvent box for the given snapshot (Figure 2). To include not only the steric, i.e., mechanical, but also electrostatic effects of the solvent,  $E_{\text{sf}}$  is calculated quantum chemically. The sum of all  $E_{\text{sf}}$  yields the solvent potential  $V_{\text{solv}}$  for this grid point (eq 3). This procedure is repeated for the whole grid, leading to a  $V_{\text{solv}}$  mapped to the coordinate space of the potential energy surface  $V_{\text{mol}}$ . The sum of both yields the total potential  $V_{\text{tot}}$  for the reaction in solution. To permit the quantum chemical calculation of  $E_{\text{sf}}$ , we precalculate the interaction between the reactant and one solvent molecule for all possible relative orientations on a regular space grid in the six-dimensional orientation space. The energy for any arbitrary orientation is then obtained by interpolation.

The QD calculations are carried out on all thus-constructed  $V_{\text{tot}}$  individually. The average of all QD simulations reflects the impact of the solvent surrounding on the investigated process. It is calculated by summation of the absolute squares of the propagated wave functions  $\Psi_i$  using the different solvent potentials of the  $N_{\text{snap}}$  snapshots

$$|\Psi_{\text{av}}|^2 = \frac{1}{N_{\text{snap}}} \sum_{i=1}^{N_{\text{snap}}} |\Psi_i|^2 \quad (4)$$

An important issue to consider is the ratio of the time scales for the motion of the reactant and the motion of the solvent

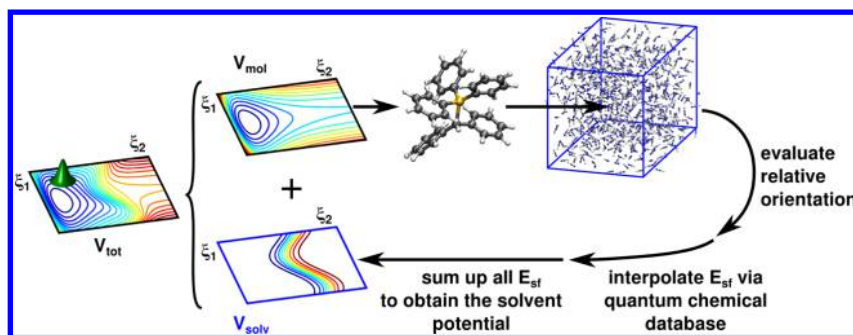


**Figure 2.** Flowchart visualizing the procedure to calculate the solvent potential  $V_{\text{solv}}$  based on the reactive coordinates  $\xi_i$  of the ab initio molecular potential  $V_{\text{mol}}$ . For all combinations of  $\xi_1$  and  $\xi_2$ , a solute molecule is placed into the cavity in the solvent box, the relative orientation between the solvent molecules and the fragments is evaluated, and  $E_{\text{sf}}$  is interpolated via the quantum chemical database. Finally, all  $E_{\text{sf}}$  are summed for each  $(\xi_1, \xi_2)$  to yield  $V_{\text{solv}}$ , which is then added to  $V_{\text{mol}}$ . The resulting  $V_{\text{tot}}$  is used for the QD simulations.

molecules. In general, three different scenarios are possible: Either the molecular reaction is much faster than the motion of the solvent molecules or vice versa or the dynamics of both systems happens on a comparable time scale. In the first two cases, one can take advantage of the separation of time scales. In case one, the position of the solvent molecules at the beginning of the molecular reaction is decisive for the whole process and, as a first approximation, the solvent motion is negligible. This is the case for ultrafast photoinduced processes on the hundreds of femtoseconds time scale, like photochemical bond cleavage<sup>5,13–15</sup> or photoisomerization.<sup>16,17</sup> In the second case, one can average over the solvent dynamics. Thus, only one solvent potential  $V_{\text{solv}}$  is experienced by the reactant. In the third case, when both dynamics are comparably fast, no separation of time scales is possible and both systems have to be propagated in parallel. An example for this case are vibrationally mediated processes involving ladder climbing<sup>18,19</sup> or bimolecular processes in the ground state.<sup>20</sup>

**2.2. Evaluating the Coordinates Relevant for the Relative Orientation of Solvent and Fragment.** The MD simulations can be used not only to take the snapshots needed for a statistical solvent description but also to facilitate rating the five rotational axes with regard to their importance for the interaction energy  $E_{\text{sf}}$ . The decisive criterion for their rating is the standard deviation  $\sigma_{q_n}$  of the probability distribution of  $E_{\text{sf}}$  for each coordinate  $q_n$ . The larger  $\sigma_{q_n}$ , the more important is the coordinate  $q_n$ . Note that the standard deviation depends on the temperature  $T$ , as each MD simulation sketches a Boltzmann distribution. Thus, the obtained rating is valid only for the given temperature  $T$ .

The standard deviation  $\sigma_{q_n}$  for a chosen coordinate  $q_n$  can be calculated starting from the empirical distribution function  $F_m(q_n)$  for a random sample of  $m$  elements<sup>21</sup>

$$F_m(q_n) = \frac{1}{m} \sum_{i=1}^m 1\{q_{ni} \leq q_n\} \quad (5)$$

with  $q_{ni}$  being the coordinate values from the random sample.  $F_m(q_n)$  is the fraction of the  $m$  elements of the sample that fulfill the condition  $q_{ni} \leq q_n$ . For the case of an infinite sample size, the derivative of  $F_m(q_n)$  is the probability distribution  $P(q_n)$

$$P(q_n) = \frac{\partial}{\partial q_n} F_m(q_n) \quad (6)$$

With the integral  $\int_{q_0}^{q_0+\Delta q} P(q_n) dq_n$ , the probability for  $q_n$  to take a value within the interval  $[q_0; q_0 + \Delta q]$  can be evaluated. The probability distribution  $P(q_n)$  is Boltzmann distributed, as it is extracted from an MD simulation at a particular temperature  $T$

$$P(q_n) = \frac{1}{Z_{q_n}} \exp\left(-\frac{E_{\text{sf}}(q_n)}{k_B T}\right) \quad (7)$$

with  $1/Z_{q_n}$  being the normalization factor and  $Z_{q_n}$  the canonical partition function. The usual degeneracy factor is not present in eq 7 because, first, it is already included due to the explicit dependence of  $E_{\text{sf}}$  on the coordinate  $q_n$ , which compensates for orientations with the same  $E_{\text{sf}}$  value. Second, all coordinate-dependent degeneracies can be removed beforehand by ensuring that each orientation is uniquely defined in the orientation space. To obtain  $E_{\text{sf}}(q_n)$ , we take the logarithm of eq 7. As for the coordinate rating, we are interested only in the relative variation of  $E_{\text{sf}}(q_n)$  along  $q_n$  and not in the absolute values, the expression can be simplified by shifting  $E_{\text{sf}}(q_n)$  by  $\ln(Z_{q_n}) k_B T$

$$\begin{aligned} E'_{\text{sf}}(q_n) &= E_{\text{sf}}(q_n) + \ln(Z_{q_n}) k_B T \\ &= -\ln(P(q_n)) k_B T \end{aligned} \quad (8)$$

Equation 8 provides an elegant way to obtain the potential landscape for the interaction energy  $E'_{\text{sf}}(q_n)$  from the MD simulation without explicit calculation. The accessibility of the different energy states depends on the temperature. Thus, the next step is the transformation of  $E'_{\text{sf}}(q_n)$  into the probability distribution  $P(E'_{\text{sf}})$ . The probability that a specific energy state is occupied is given by the Boltzmann distribution, where the density of states  $n(E'_{\text{sf}})$  takes the place of the degeneracy factor

$$P(E'_{\text{sf}}) = \frac{1}{Z_{E'_{\text{sf}}}} \exp\left(-\frac{E'_{\text{sf}}}{k_B T}\right) n(E'_{\text{sf}}) \quad (9)$$

with  $Z_{E'_{\text{sf}}}$  being the canonical partition function. The density of states is the sum of the reciprocal absolute gradients of  $E'_{\text{sf}}(q_n)$  at all values of  $q_n$  for which  $E'_{\text{sf}}(q_n) = E'_{\text{sf}}$  multiplied by  $N(q_n)$

$$n(E'_{\text{sf}}) = \sum_{E'_{\text{sf}}(q_n) = E'_{\text{sf}}} \left| \frac{\partial E'_{\text{sf}}(q_n)}{\partial q_n} \right|^{-1} N(q_n) \quad (10)$$

$N(q_n)$  is a coordinate-dependent degeneracy factor. For the spherical coordinates, as used here to describe the relative



orientation between the fragments and the solvent, the factor takes into account the different accessible surface areas of a sphere depending on the polar angle.

Figure 3a shows an exemplary probability distribution  $P(q_n)$  along an angular coordinate  $q_n$ . Following eq 8, we extract the

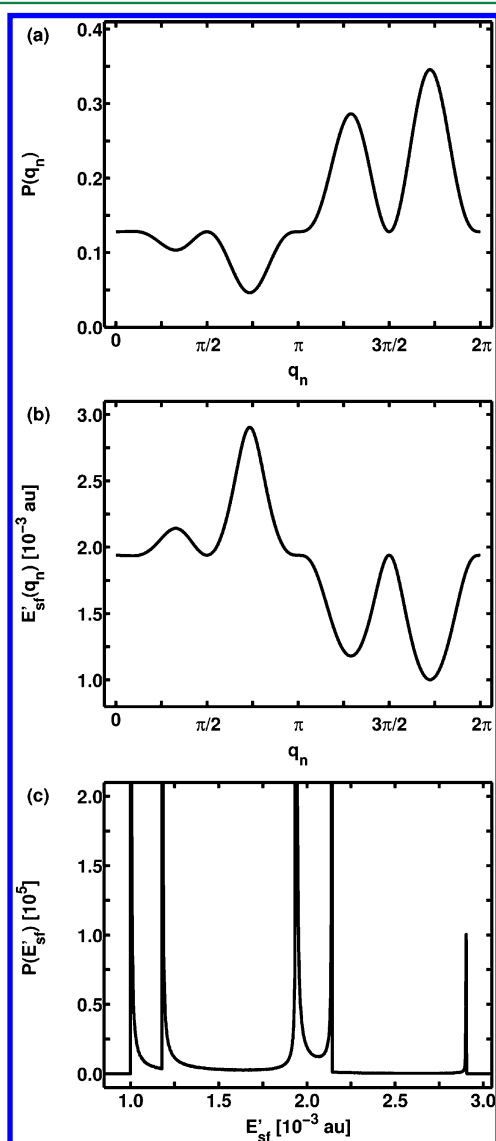


**Figure 3.** (a) Probability distribution  $P(q_n)$  along an angular coordinate  $q_n$ . (b)  $E'_{sf}(q_n)$  along  $q_n$  calculated from  $P(q_n)$  at a temperature of  $T = 298$  K according to eq 8. As expected, the maxima in the probability distribution  $P(q_n)$  correspond to minima in  $E'_{sf}(q_n)$ . (c) Probability distribution for the energy  $P(E'_{sf})$  resulting from  $E'_{sf}(q_n)$  depicted in (b) at  $T = 298$  K determined according to eq 9.

underlying  $E'_{sf}(q_n)$  (Figure 3b). As expected, the maxima in  $P(q_n)$  correspond to minima in  $E'_{sf}(q_n)$ . The probability distribution  $P(E'_{sf})$  is calculated from eq 9 and depicted in Figure 3c. It shows the typical structure of a density of states. The stationary points of  $E'_{sf}(q_n)$  lead to the poles of  $P(E'_{sf})$  due to the reciprocal absolute gradient in eq 10. The broader the energy range of  $P(E'_{sf})$ , the larger the standard deviation  $\sigma_{q_n}$  gets. In Figure 3c, the most relevant range is from  $1 \times 10^3$  to  $2.2 \times 10^3$  au. With the expectation value of the energy  $\overline{E'_{sf}}$

$$\overline{E'_{sf}} = \int_{-\infty}^{\infty} E'_{sf} \cdot P(E'_{sf}) dE'_{sf} \quad (11)$$

finally, the standard deviation  $\sigma_{q_n}$  can be calculated as the square root of the variance  $\text{Var}(E'_{sf})$

$$\sigma_{q_n} = \sqrt{\text{Var}(E'_{sf})} = \sqrt{\int_{-\infty}^{\infty} (E'_{sf} - \overline{E'_{sf}})^2 P(E'_{sf}) dE'_{sf}} \quad (12)$$

### 3. COMPUTATIONAL DETAILS

For all MD simulations, the program package Gromacs<sup>22,23</sup> (version 3.3.2) was used. The solute  $\text{Ph}_2\text{CH}-\text{PPh}_3^+$  was described by the all-atom version of the OPLS (optimized potentials for liquid simulations) force field.<sup>24</sup> The atomic charges were determined quantum chemically (DFT, M06-2X, 6-31G(d)) with the program package Gaussian09.<sup>25</sup> For the liquid MeCN, force field parameters developed by Edwards et al.<sup>26</sup> were used that reproduced the viscosity of MeCN well.<sup>27</sup> We used a cubic simulation box with an edge length of 40 Å containing 709 MeCN molecules. The time evolution was calculated using a time step of 1 fs. The temperature was kept constant at 298 K by a Berendsen thermostat. After propagating the system for 10 ps while monitoring the temperature to ensure successful equilibration, snapshots were taken every 200 fs.

The interaction energy  $E_{sf}$  between a fragment and a MeCN molecule was evaluated quantum-chemically at the DFT (M06-2X, 6-31G(d)) level of theory with the program package Gaussian09.<sup>25</sup> The molecular potential  $\hat{V}_{\text{mol}}$  of  $\text{Ph}_2\text{CH}-\text{PPh}_3^+$  was calculated with the our own  $n$ -layered integrated molecular orbital and molecular mechanics (ONIOM) method.<sup>28–30</sup> The high-level system (thicker drawn part of  $\text{Ph}_2\text{CH}-\text{PPh}_3^+$  in Figure 4, top) was calculated at the CASSCF(10,10) level of theory with the program package Molpro;<sup>31</sup> the low-level system additionally contains the thinner phenyl rings and is calculated at the DFT (M06-2X) level of theory using Gaussian09.<sup>25</sup> Throughout all calculations, the basis set 6-31G(d) was employed. This approach was already employed and tested in ref 5. The coordinates for the quantum dynamical calculations are the C1–P distance  $r$  and the angle  $\phi$  between the atoms P, C1, and the dummy atom X, which is introduced to ensure that the conical intersection (CoIn) lies in the coordinate space. Along the dissociation coordinate  $r$ , which describes the distance between the phosphorus atom P and the carbon atom C1 (Figure 4, top), the potential energy surface accounts for the major relaxation processes. Those are given by the lowering of the hybridization from  $\text{sp}^3$  to  $\text{sp}^2$  at the C1 atom of the methyl group as well as the rotation of the phenyl rings and bond length changes.

The quantum dynamical simulations were carried out by a homemade program that solves the time-dependent Schrödinger equation on a spatial grid using the Chebychev propagation scheme<sup>32</sup> and the G-matrix method for the kinetic operator  $\hat{T}$ <sup>33–35</sup> (for details, see the Supporting Information). At the beginning of the propagation, the vibrational ground state wave function  $v = 0$  of the electronic ground state  $S_0$  was placed on the  $S_1$  state. It was shifted slightly to a shorter C1–P distance to ensure that the main part of the wave packet crosses the barrier next to the Franck–Condon (FC) region in the gas phase. This is necessary because the two-dimensional coordinate space does not include the minimal barrier.<sup>36</sup> To include it, a third coordinate would be required, which would lead to an enormous increase in the simulation time.

#### 4. BOND CLEAVAGE OF $\text{Ph}_2\text{CH}-\text{PPh}_3^+$ IN AN EXPLICIT SOLVENT ENVIRONMENT

Our interest lies in the photochemistry of medium-sized organic molecules, in particular in photoinduced dissociative processes. A well-suited example for the significance of the dynamic solvent effect is the bond cleavage of  $\text{Ph}_2\text{CH}-\text{PPh}_3^+$  in MeCN<sup>4,5</sup> for which we apply our new QD/MD approach. Salts like  $\text{Ph}_2\text{CH}-\text{PPh}_3^+\text{X}^-$  are common precursors for the generation of diphenylmethyl cations ( $\text{Ph}_2\text{CH}^+$ ) as intermediates in polar and moderately polar solvents (Figure 4).<sup>37</sup>

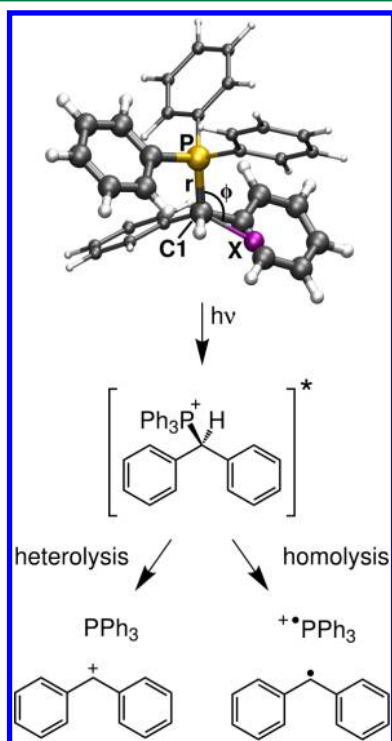


**Figure 4.** Reaction scheme for the photochemical bond cleavage in diphenylmethyltriphenylphosphonium ions  $\text{Ph}_2\text{CH}-\text{PPh}_3^+$ . The ground state has heterolytic dissociation character, leading to  $\text{Ph}_2\text{CH}^+$  and  $\text{PPh}_3$  as photoproducts; the character of the first and second excited state is homolytic, generating  $\text{Ph}_2\text{CH}^\bullet$  and  $\text{PPh}_3^{\bullet+}$ . The optimized geometry of  $\text{Ph}_2\text{CH}-\text{PPh}_3^+$  is depicted at the top. The potential energy surface used in the quantum dynamical simulations is calculated at the ONIOM level of theory. The high-level system  $\text{PhCH}_2-\text{Ph}_2\text{Ph}^+$  of the ONIOM calculations contains the thicker drawn part of  $\text{Ph}_2\text{CH}-\text{PPh}_3^+$ ; in the low-level system  $\text{Ph}_2\text{CH}-\text{PPh}_3^+$ , the thinner drawn phenyl rings are taken into account additionally. The coordinates for the quantum dynamical calculations are the C1–P distance  $r$  and the angle  $\phi$  between the atoms P, C1, and the dummy atom X, which is introduced to ensure that the CoIn lies in the coordinate space.

Ultrafast broadband transient absorption experiments revealed that almost exclusively diphenylmethyl cations are formed if the counterion  $\text{X}^-$  is nonoxidizable (e.g.,  $\text{BF}_4^-$  or  $\text{SbF}_6^-$ ).<sup>38</sup> Quantum chemical investigations showed that after a local  $\pi-\pi^*$  excitation on the  $\text{PPh}_3$  moiety the C1–P bond cleavage can take place by crossing a small barrier in the first excited state  $\text{S}_1$ .<sup>36</sup> In the dissociation limit, the  $\text{S}_1$  state leads to the formation of a radical pair  $\text{Ph}_2\text{CH}^\bullet$  and  $\text{PPh}_3^{\bullet+}$  (homolytic bond cleavage), whereas in the ground state  $\text{S}_0$ , the desired  $\text{Ph}_2\text{CH}^+$  cations and  $\text{PPh}_3$  are generated (heterolytic bond cleavage). QD simulations clarified that for the bond cleavage

in  $\text{Ph}_2\text{CH}-\text{PPh}_3^+$  ions the dynamic solvent effect is essential. By including the frictional force of the solvent implicitly, we were able to explain the experimentally observed initial product formation on the several hundreds of femtoseconds time scale.<sup>4,5,38</sup> The applied dynamic continuum ansatz combines Stokes' law with the dynamic viscosity of the solvent to model the deceleration by the solvent cage.<sup>5</sup> This enables the system to reach a CoIn, which connects both product channels and allows the fast generation of  $\text{Ph}_2\text{CH}^+$  cations.<sup>5</sup>

The presented QD/MD approach goes one step further and includes an atomistic modeling of the solvent cage. Here, the MeCN solvent cage is obtained from MD simulations, during which the methyl group of MeCN is treated as a united atom.<sup>26</sup> If the bending is neglected, then MeCN can be treated as linear. One advantage of this simplification is that the number of coordinates in the orientation space can be reduced to five if one of the rotational axes of MeCN is selected to be collinear with the molecular axis. During the QD calculations, the positions of the solvent molecules around the solute  $\text{Ph}_2\text{CH}-\text{PPh}_3^+$  are frozen, as in scenario one (introduced in Section 2.1). This is legitimized by the fact that the bond cleavage takes place within 200–300 fs and is faster than the motion of the solvent molecules in the thermodynamic equilibrium. Thus, the initially experienced solvent potential  $V_{\text{solv}}$  is crucial for the time evolution of the wave packet, although the shape of the solvent cage will change during the reaction process.

The five coordinates  $|\vec{r}_{\text{sf}}|$ ,  $\alpha_s$ ,  $\alpha_f$ ,  $\beta_s$ , and  $\beta_f$  to describe  $E_{\text{sf}}$  in the orientation space are presented in Figure 5.  $|\vec{r}_{\text{sf}}|$  is the

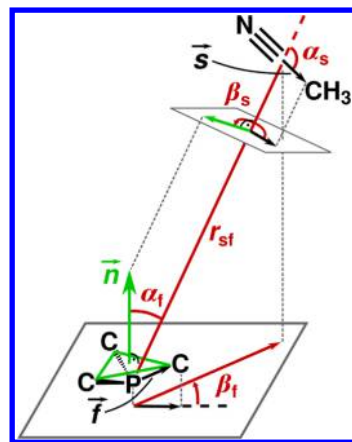


**Figure 5.** Definition of the five coordinates  $r_{\text{sf}}$ ,  $\alpha_s$ ,  $\alpha_f$ ,  $\beta_s$ , and  $\beta_f$  describing the relative orientation of one MeCN and the  $\text{PPh}_3$  moiety. For the sake of simplicity, only the C atoms of the phenyl rings that are bound to the P atom are shown; the remaining atoms are omitted.

length of the connecting vector between the center of mass of MeCN and the central atom of the two fragments: the P atom in the case of  $\text{PPh}_3$  and the methyl C atom for  $\text{Ph}_2\text{CH}$ . The remaining four coordinates are angles describing the rotation of the fragment ( $\alpha_f$ ,  $\beta_f$ ) and of the solvent ( $\alpha_s$ ,  $\beta_s$ ). In detail,  $\alpha_f$  specifies the angle between  $\vec{r}_{\text{sf}}$  and the normal vector  $\vec{n}$  of the plane (green triangle) defined by the three C atoms attached to the P atom. It is defined in the interval  $[0; \pi]$ .  $\beta_f$  characterizes the rotation of the  $\text{PPh}_3$  fragment around  $\vec{n}$ . To this, we use the auxiliary vector  $\vec{f}$ , which points from the P atom to one C atom.  $\beta_f$  is then defined as the angle (counterclockwise) between the projections of the vectors  $\vec{r}_{\text{sf}}$  and  $\vec{f}$  into the

C–C–C plane. The angle  $\beta_f$  takes values between  $[0; 2\pi[$ .  $\alpha_s$  is the angle between  $\vec{r}_{sf}$  and the vector  $\vec{s}$ , which points from the center of mass of MeCN to its methyl group. The angle  $\alpha_s$  is defined in the interval  $[0; \pi]$ .  $\beta_s$  indicates the rotation of MeCN around  $\vec{r}_{sf}$  and is defined in the interval  $[0; 2\pi[$ . It is calculated projecting the vectors  $\vec{s}$  and  $\vec{n}$  into a plane perpendicular to  $\vec{r}_{sf}$ . The angle between these projected vectors (again in counter-clockwise direction) is  $\beta_s$ . For the second fragment, Ph<sub>2</sub>CH, generated in the bond cleavage, the methyl C atom replaces the P atom and one atom of the C–C–C plane is exchanged by the H atom. The selected coordinates are orthogonal and guarantee that each position in the orientation space is uniquely defined by one coordinate quintuple.

In the next step, the importance of the five coordinates for the interaction energy  $E_{sf}$  has to be evaluated. The significance of the distance coordinate is obvious; the rating of the four angular coordinates has to be determined according to the standard deviations  $\sigma_{q_n}$ . For this, 2500 snapshots along MD trajectories were analyzed. The orientations of all MeCN molecules with a maximum distance of 8.0 Å between the two nearest atoms of the fragment and the solvent molecule were calculated. Beyond 8.0 Å, no influence of the structure of the solute on the solvent orientation was observed. As  $E_{sf}$  depends on all five coordinates, orientational effects along one coordinate can be compensated by another one. This happens when the preferred value for one coordinate depends systematically on the value of one or more other coordinates. To ensure that no compensation of orientations occurs for the tested coordinate, we divided the interval of the remaining angular coordinates in half and compared the shape of the obtained probability distributions  $P(q_n)$  of both parts with each other and the initial shape. If they are similar enough, then no further dividing is necessary; if they are not, then the procedure is repeated for both halves. When convergence of the shape is reached in step  $i$ , the  $(i - 1)$ th partitioning is used to calculate the  $m$  related standard deviations  $\sigma_{q_n}^i$  for the  $m$  resulting intervals with  $j \in \{1, 2, \dots, m\}$ . The standard deviation  $\sigma_{q_n}$  for the whole domain of definition is calculated via the average of the variances  $(\sigma_{q_n}^i)^2$  weighted by the proportion of elements  $N_j/N_0$  in the interval  $j$  according to

$$\sigma_{q_n} = \sqrt{\sum_{j=1}^m \frac{N_j}{N_0} (\sigma_{q_n}^j)^2} \quad (13)$$

where  $N_j$  is the number of elements in the interval  $j$  and  $N_0 = \sum_{j=1}^m N_j$  (for details, see the Supporting Information). As the probability distributions are quite noisy, a comparison of the raw data is difficult. Thus,  $P(q_n)$  was smoothed by applying a low-pass Butterworth filter before being normalized. Additionally, we calculated the integral of the absolute difference of the normalized probability distributions to check that the absolute deviations are not too large. All values were below 12% (for details, see the Supporting Information).

The values of the standard deviations  $\sigma_{q_n}$  along the four angular coordinates calculated following eq 13 are given in Table 1. Their values are between  $7.21 \times 10^{-5}$  and  $2.71 \times 10^{-4}$  au. In general, the ones for the PPh<sub>3</sub> moiety are slightly larger than the ones for Ph<sub>2</sub>CH. This could be due to the less sterically demanding H atom that replaces one phenyl ring, which leads to a flatter potential around the H atom and thus

**Table 1.** Standard Deviation  $\sigma_{q_n}$  of the Interaction Energy between the Molecular Fragment and MeCN along the Four Angular Coordinates  $\alpha_s$ ,  $\beta_s$ ,  $\alpha_\phi$  and  $\beta_f$

fragment	$\sigma_{\alpha_s}$ (au)	$\sigma_{\beta_s}$ (au)	$\sigma_{\alpha_\phi}$ (au)	$\sigma_{\beta_f}$ (au)
PPh <sub>3</sub>	$1.58 \times 10^{-4}$	$7.61 \times 10^{-5}$	$1.62 \times 10^{-4}$	$2.71 \times 10^{-4}$
Ph <sub>2</sub> CH	$1.28 \times 10^{-4}$	$7.21 \times 10^{-5}$	$1.03 \times 10^{-4}$	$1.34 \times 10^{-4}$

reduces the standard deviation in the probability distributions  $P(E_{sf})$ . We carefully checked the influence of the filtering process on the values of  $\sigma_{q_n}$ . They change slightly, but the observed trends are fairly robust.

For the PPh<sub>3</sub> moiety,  $\sigma_{\beta_s}$  has the smallest value. The other values are at least twice as large; the largest one is observed for  $\sigma_{\beta_f}$ . A similar picture is obtained for the Ph<sub>2</sub>CH moiety. Here also,  $\sigma_{\beta_s}$  has the smallest value. Since for both fragments  $\sigma_{\beta_s}$  has the smallest value,  $\beta_s$  is the least important coordinate for the interaction energy  $E_{sf}$ . As the  $E_{sf}$  values entering the QD simulations are evaluated quantum chemically, the reduction of its degrees of freedom from  $n = 5$  to  $n = 4$  leads to a significant reduction in computational time. Thus, the solvent potential  $\hat{V}_{\text{solv}}(r, \phi)$  is approximated as

$$\hat{V}_{\text{solv}}(r, \phi) = \sum_{i=1}^{N_{\text{solv}}} \sum_{j=1}^2 E_{sf} \left( \left| \vec{r}_{sf}^{ij}(r, \phi) \right|, \alpha_s^{ij}(r, \phi), \alpha_\phi^{ij}(r, \phi), \beta_f^{ij}(r, \phi) \right) \quad (14)$$

We calculated  $V_{\text{solv}}(r, \phi)$  for 50 snapshots of the MD trajectories with a time interval of 200 fs between the snapshots and simulated the bond cleavage process quantum dynamically for each of the obtained  $V_{\text{tot}}$ . For reference, we show the molecular potential  $V_{\text{mol}}(r, \phi)$  of the first excited state  $S_1$  without any solvent influence in Figure 6. The FC point is

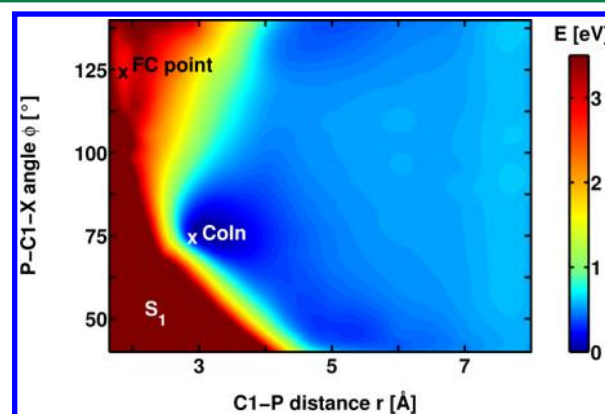


**Figure 6.** Molecular potential  $V_{\text{mol}}$  of the first excited state  $S_1$  of Ph<sub>2</sub>CH–PPh<sub>3</sub><sup>+</sup> calculated at the ONIOM (CASSCF(10,10)/M06-2X/6-31G(d)) level of theory. The potential is shown up to a C1–P distance of  $r = 8.0$  Å to clarify that  $V_{\text{mol}}$  has no barrier along the  $r$  direction.

located at a C1–P distance of  $r = 1.87$  Å and a P–C1–X angle of  $\phi = 125^\circ$ , the  $S_0/S_1$  CoIn at  $r = 2.9$  Å and  $\phi = 75^\circ$ ,<sup>5</sup> and the global  $S_1$  minimum next to the  $S_0/S_1$  CoIn.

The left column of Figure 7 depicts two selected MD snapshots. The solute Ph<sub>2</sub>CH–PPh<sub>3</sub><sup>+</sup> is drawn in a space-filling representation; the MeCN solvent molecules are shown in a ball and stick representation. The white ball represents the



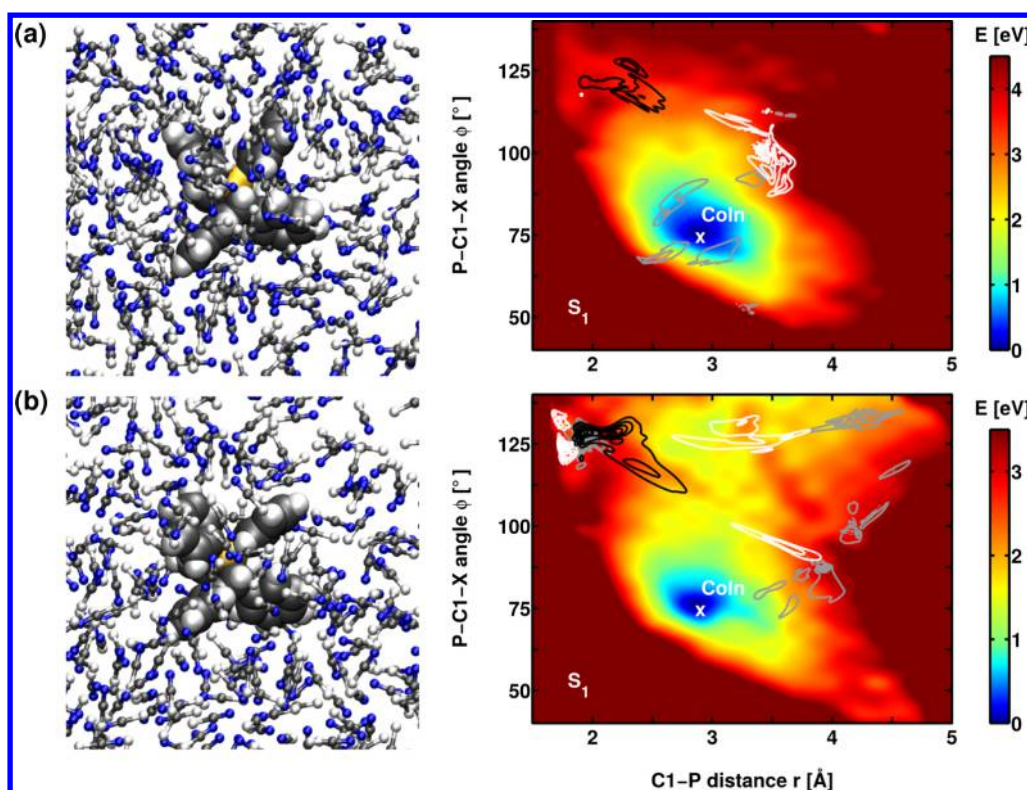


**Figure 7.** Two selected snapshots of  $\text{Ph}_2\text{CH-PPh}_3^+$  in a box of MeCN taken from the MD simulation (left column). The solute  $\text{Ph}_2\text{CH-PPh}_3^+$  is drawn in a space-filling representation; the MeCN solvent molecules are shown in a ball and stick representation. The white ball represents the methyl group, the gray one the C atom and the blue one the N atom. The corresponding total potentials  $V_{\text{tot}}(r, \phi)$  are depicted in the right column together with three snapshots of the propagated wave packets. For (a), they are taken at 90 fs (black isolines), 180 fs (white isolines), and 240 fs (gray isolines), and for (b), at 90 fs (black isolines), 160 fs (white isolines), and 240 fs (gray isolines) after starting the propagation in the FC region. In the total potential  $V_{\text{tot}}$  shown in (a), the whole wave packet explores the channel toward the global minimum and oscillates around the CoIn. In contrast, the wave packet in  $V_{\text{tot}}$  depicted in (b) splits and explores both offered dissociation pathways.

methyl group, the gray one the C atom and the blue one the N atom. The right column of Figure 7 shows the total potential  $V_{\text{tot}}$  of the first excited state  $S_1$  for the depicted solvent arrangements together with three snapshots from the wave packet evolution. The snapshots in Figure 7a are taken at 90 fs (black isolines), 180 fs (white isolines), and 240 fs (gray isolines), and in Figure 7b, at 90 fs (black isolines), 160 fs (white isolines), and 240 fs (gray isolines) after starting the propagation in the FC region of the  $S_1$  state.

First, we focus on the two resulting  $V_{\text{tot}}$ , which exhibit significant differences in their topography. The solvent potential generates a barrier at large C1-P distances of approximately  $r = 3.5$  Å, where the dissociating fragments approach the solvent cage. This leads to the steep rise of the total potential, which is not present in the purely molecular potential  $V_{\text{mol}}$  (Figure 6). The first  $V_{\text{tot}}$  (Figure 7a, right) has one valley pointing toward the CoIn. In contrast, the second  $V_{\text{tot}}$  (Figure 7b, right) offers two reaction channels. One points toward the CoIn, and the other one leads away from the CoIn. These examples represent the two limiting cases found in the 50 snapshots taken from the MD trajectories. The first case occurs about two times more often than the second.

The quantum dynamics of the bond cleavage is visualized by the selected snapshots from the wave packet propagation. In Figure 7a, the wave packet leaves the FC area about 90 fs after the propagation has been started (black isolines). Subsequently, it hits the potential barrier of the solvent cage at about  $r = 3.7$  Å and  $\phi = 100^\circ$  (white isolines). Then, it evolves toward the

CoIn and oscillates back and forth around the global minimum of  $V_{\text{tot}}$ . The time evolution of the wave packet in the second solvent arrangement (Figure 7b) differs fundamentally. After 90 fs, a part of the wave packet crosses the barrier in the FC region and moves toward a larger C1-P distance (black isolines). Compared to the propagation in Figure 7a, a significant fraction stays in the FC minimum. The part overcoming the barrier already reveals a splitting toward the two reaction channels. At 160 fs, the branching of the wave packet is completed (white isolines). The upper fraction moves toward larger  $\phi$  values and dissociates in the first excited state, leading to the formation of radicals (gray isolines). The lower part hits the potential barrier at around  $r = 4.0$  Å and  $\phi = 90^\circ$  and is guided toward the CoIn with the ground state.

The two examples demonstrate the importance of the individual arrangement of the solvent cage. It has a significant impact on the direction in which the wave packet evolves and whether a splitting occurs. The second reaction channel opens when no solvent molecules hinder the motion of the reactant along that channel. This situation can be captured only by a microscopic description of the solvent environment, as provided by our QD/MD ansatz.

For an overall picture of the bond cleavage, we averaged the wave packet propagations for the 50 different environments according to eq 4. As we found convergence in the population dynamics, 50 snapshots proved to be a sufficiently large number (for details, see the Supporting Information). To analyze the population distribution, we separated the two-dimensional

potentials in three areas. They correspond to the FC region ( $r \leq 2.1$  Å and  $\phi > 105^\circ$ ; gray rectangle in the inset of Figure 8),

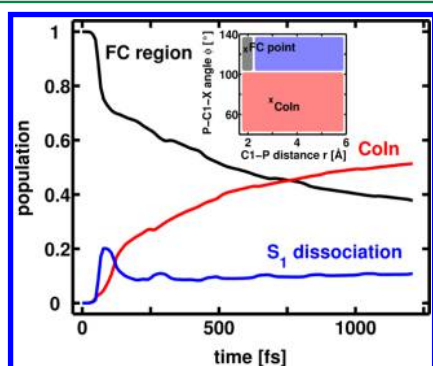


**Figure 8.** Population dynamics for the QD simulation of the bond cleavage of  $\text{Ph}_2\text{CH-PPh}_3^+$  averaged over 50 different solvent arrangements taken from MD trajectories. The population in the FC region (black line) is located in the gray rectangle in the inset, the population in the  $S_1$  dissociation area (blue line) in the blue rectangle, and the population around the CoIn (red line) in the red rectangle.

the dissociation channel in the  $S_1$  state ( $r > 2.1$  Å and  $\phi > 105^\circ$ ; blue rectangle), and the area around the CoIn ( $\phi \leq 105^\circ$ ; red rectangle). To start the propagation, the vibrational ground state wave function  $\nu = 0$  is transferred to the  $S_1$  state. Accordingly, the population in the FC region is one at  $t = 0$  fs (black line). Within the first 70 fs, 30% of the population leave the FC region with an initial momentum along the  $r$  direction, observable in the sudden increase of population in the  $S_1$  dissociation channel (blue line). At about 100 fs, the averaged wave packet is deflected toward the CoIn. Correspondingly, the population now increases in this area (red line). This increase continues moderately while the  $S_1$  dissociation channel stays constant. After 1200 fs, the population is distributed as follows: 40% is still located in the FC region, 10% dissociated in the first excited state, and 50% reached the CoIn, from where the population can relax to the ground state<sup>5,36</sup> to form the experimentally observed  $\text{Ph}_2\text{CH}^+$  cations. The explicit treatment of the solvent provides a passage toward the CoIn similar to the results from the dynamic continuum ansatz.<sup>5</sup> Furthermore, it captures the individual arrangements of the solvent cage and, based on this, reveals the formation of different reaction channels.

## 5. SUMMARY AND CONCLUSIONS

We presented our newly developed QD/MD method to include the explicit solvent environment in reactive QD simulations. The method merges MD simulations of the reactant in a box of solvent molecules with QD calculations of the reactant's dynamics. The interaction between the QD system and the solvent molecules is incorporated in the Hamiltonian for the QD calculations. The interaction energy  $E_{\text{sf}}$  between the reactant and a solvent molecule depends on their relative orientation, which, in general, can be described by six degrees of freedom  $q_n$  with  $n \in \{1, 2, \dots, 6\}$  in the orientation space. We showed that MD trajectories also provide the necessary information to calculate the standard deviation  $\sigma_{q_n}$  of the interaction energy  $E_{\text{sf}}(q_n)$  as a decisive criterion for rating the coordinates  $q_n$ . With this procedure, the least relevant degrees of freedom can be eliminated to reduce the

computational cost for the precalculation of the quantum chemical database.

To demonstrate the impact of the solvent cage treated explicitly with our new QD/MD approach, we chose the photoinduced bond cleavage of  $\text{Ph}_2\text{CH-PPh}_3^+$ . It has been shown that consideration of dynamic solvent effects during the quantum dynamical simulation of the process is crucial to explain the experimentally observed heterolytic bond cleavage generating  $\text{Ph}_2\text{CH}^+$  cations.<sup>5,38</sup> We performed MD simulations of one  $\text{Ph}_2\text{CH-PPh}_3^+$  in a box of MeCN. The rating of the coordinates in the orientation space led to four necessary coordinates: the distance coordinate  $r_{\text{sf}}$  and three angular coordinates  $\alpha_s$ ,  $\alpha_b$ , and  $\beta_r$ . With them, we calculated the solvent potential  $V_{\text{sol}}(r, \phi)$  for 50 snapshots of the MD simulations and performed QD simulations for each of the obtained total potentials  $V_{\text{tot}}(r, \phi)$ . The solvent cage hinders the free dissociation in the  $S_1$  state. In the microscopic description, two different dissociation channels emerged. One leads to dissociation in the  $S_1$  state and homolytic bond cleavage, and the other one leads to a  $S_0/S_1$  CoIn, where the system can relax to the ground state, which has heterolytic dissociation character. The average over all QD simulations gives the overall picture of the photoinduced bond cleavage. 83% of the excited state population that leaves the FC region approaches the CoIn, where the formation of  $\text{Ph}_2\text{CH}^+$  cations can take place. The remaining 17% pass through the second dissociation channel of the homolytic bond cleavage. Thus, our new QD/MD approach provides a passage toward the CoIn similar to the results from the dynamic continuum ansatz<sup>5</sup> and explains the experimental observations for the initial product formation.<sup>38</sup> Compared to the dynamic continuum ansatz, it goes one step further and gives a more detailed microscopic picture of the whole process. It allows for the description of different reaction channels reflecting the individual arrangements of the solvent cage. Furthermore, the flexibility of the solvent cage with temperature and solvent composition can be modeled.

The presented results demonstrate encouragingly that a combination of MD and QD simulations is an appropriate tool to describe photoinduced ultrafast molecular processes in a complex environment. The next step for future development is the inclusion of the feedback of the QD system on the motion of the classically treated solvent molecules. This will further broaden the application range to reactions where the dynamics of the reactant and solvent are on a comparable time scale.

## ■ ASSOCIATED CONTENT

### Supporting Information

Details of the quantum dynamical simulations, the partitioning of the coordinates in the orientation space to calculate the probability distributions  $P(q_n)$ , the convergence of the population dynamics, a qualitative comparison of the required computing time, and geometries in xyz format. This material is available free of charge via the Internet at <http://pubs.acs.org>.

## ■ AUTHOR INFORMATION

### Corresponding Author

\*E-mail: [regina.de\\_vivie@cup.uni-muenchen.de](mailto:regina.de_vivie@cup.uni-muenchen.de).

### Funding

Financial support by the Deutsche Forschungsgemeinschaft through SFB749 and the excellence cluster Munich-Centre for Advanced Photonics (MAP) is acknowledged.



## Notes

The authors declare no competing financial interest.

## ■ ACKNOWLEDGMENTS

We thank Eberhard Riedle for fruitful discussions and Andrea Kreppel for carrying out first test calculations. S.T. thanks the Dr. Klaus Römer-Stiftung for financial support.

## ■ REFERENCES

- (1) Reichardt, C.; Welton, T. *Solvents and Solvent Effects in Organic Chemistry*; Wiley-VCH: Weinheim, Germany, 2011.
- (2) Sailer, C. F.; Thallmair, S.; Fingerhut, B. P.; Nolte, C.; Ammer, J.; Mayr, H.; de Vivie-Riedle, R.; Pugliesi, I.; Riedle, E. *ChemPhysChem* **2013**, *14*, 1423–1437.
- (3) Struebing, H.; Ganase, Z.; Karamertzanis, P. G.; Siougkrou, E.; Haycock, P.; Piccione, P. M.; Armstrong, A.; Galindo, A.; Adjiman, C. S. *Nat. Chem.* **2013**, *5*, 952–957.
- (4) Thallmair, S.; Kowalewski, M.; Fingerhut, B.; Sailer, C.; de Vivie-Riedle, R. *EPJ Web Conf.* **2013**, *41*, 05043–1–05043–3.
- (5) Thallmair, S.; Kowalewski, M.; Zauleck, J. P. P.; Roos, M. K.; de Vivie-Riedle, R. *J. Phys. Chem. Lett.* **2014**, *5*, 3480–3485.
- (6) Benjamin, I.; Wilson, K. R. *J. Chem. Phys.* **1989**, *90*, 4176–4197.
- (7) Krylov, A. I.; Gerber, R. B. *J. Chem. Phys.* **1994**, *100*, 4242–4252.
- (8) Amatatsu, Y.; Morokuma, K. *Chem. Phys. Lett.* **1995**, *245*, 469–474.
- (9) Winter, N.; Chorny, I.; Vieceli, J.; Benjamin, I. *J. Chem. Phys.* **2003**, *119*, 2127–2143.
- (10) Moskun, A. C.; Jailaubekov, A. E.; Bradforth, S. E.; Tao, G.; Stratt, R. M. *Science* **2006**, *311*, 1907–1911.
- (11) Horng, M. L.; Gardecki, J. A.; Papazyan, A.; Maroncelli, M. *J. Phys. Chem.* **1995**, *99*, 17311–17337.
- (12) Caricato, M.; Mennucci, B.; Tomasi, J.; Ingrosso, F.; Cammi, R.; Corni, S.; Scalmani, G. *J. Chem. Phys.* **2006**, *124*, 124520-1–124520-13.
- (13) Moskun, A. C.; Bradforth, S. E. *J. Chem. Phys.* **2003**, *119*, 4500–4515.
- (14) Sailer, C. F.; Krebs, N.; Fingerhut, B. P.; de Vivie-Riedle, R.; Riedle, E. *EPJ Web Conf.* **2013**, *41*, 05042-1–05042-3.
- (15) Cui, G.; Thiel, W. *Angew. Chem., Int. Ed.* **2013**, *52*, 433–436.
- (16) Nenov, A.; Cordes, T.; Herzog, T. T.; Zinth, W.; de Vivie-Riedle, R. *J. Phys. Chem. A* **2010**, *114*, 13016–13030.
- (17) Weingart, O.; Lan, Z.; Koslowski, A.; Thiel, W. *J. Phys. Chem. Lett.* **2011**, *2*, 1506–1509.
- (18) Gollub, C.; Kowalewski, M.; Thallmair, S.; de Vivie-Riedle, R. *Phys. Chem. Chem. Phys.* **2010**, *12*, 15780–15787.
- (19) von den Hoff, P.; Thallmair, S.; Kowalewski, M.; Siemering, R.; de Vivie-Riedle, R. *Phys. Chem. Chem. Phys.* **2012**, *14*, 14460–14485.
- (20) Fingerhut, B. P.; Sailer, C. F.; Ammer, J.; Riedle, E.; de Vivie-Riedle, R. *J. Phys. Chem. A* **2012**, *116*, 11064–11074.
- (21) Bronstein, I. N.; Semendjajew, K. A.; Musiol, G.; Mühlig, H. *Taschenbuch der Mathematik*, 7th ed.; Wissenschaftlicher Verlag Harri Deutsch GmbH: Frankfurt am Main, Germany, 2008.
- (22) Lindahl, E.; Hess, B.; van der Spoel, D. *J. Mol. Model.* **2001**, *7*, 306–317.
- (23) van der Spoel, D.; Lindahl, E.; Hess, B.; Groenhof, G.; Mark, A. E.; Berendsen, H. J. C. *J. Comput. Chem.* **2005**, *26*, 1701–1718.
- (24) Jorgensen, W. L.; Maxwell, D. S.; Tirado-Rives, J. *J. Am. Chem. Soc.* **1996**, *118*, 11225–11236.
- (25) Frisch, M. J.; Trucks, G. W.; Schlegel, H. B.; Scuseria, G. E.; Robb, M. A.; Cheeseman, J. R.; Scalmani, G.; Barone, V.; Mennucci, B.; Petersson, G. A.; Nakatsuji, H.; Caricato, M.; Li, X.; Hratchian, H. P.; Izmaylov, A. F.; Bloino, J.; Zheng, G.; Sonnenberg, J. L.; Hada, M.; Ehara, M.; Toyota, K.; Fukuda, R.; Hasegawa, J.; Ishida, M.; Nakajima, T.; Honda, Y.; Kitao, O.; Nakai, H.; Vreven, T.; Montgomery, J. A., Jr.; Peralta, J. E.; Ogliaro, F.; Bearpark, M.; Heyd, J. J.; Brothers, E.; Kudin, K. N.; Staroverov, V. N.; Kobayashi, R.; Normand, J.; Raghavachari, K.; Rendell, A.; Burant, J. C.; Iyengar, S. S.; Tomasi, J.; Cossi, M.; Rega, N.; Millam, J. M.; Klene, M.; Knox, J. E.; Cross, J. B.; Bakken, V.; Adamo, C.; Jaramillo, J.; Gomperts, R.; Stratmann, R. E.; Yazyev, O.; Austin, A. J.; Cammi, R.; Pomelli, C.; Ochterski, J. W.; Martin, R. L.; Morokuma, K.; Zakrzewski, V. G.; Voth, G. A.; Salvador, P.; Dannenberg, J. J.; Dapprich, S.; Daniels, A. D.; Farkas, O.; Foresman, J. B.; Ortiz, J. V.; Cioslowski, J.; Fox, D. J. *Gaussian 09*, revision A.02; Gaussian, Inc.: Wallingford, CT, 2009.
- (26) Edwards, D. M.; Madden, P. A.; McDonald, I. R. *Mol. Phys.* **1984**, *51*, 1141–1161.
- (27) Mountain, R. D. *J. Chem. Phys.* **1997**, *107*, 3921–3923.
- (28) Svensson, M.; Humbel, S.; Froese, R. D. J.; Matsubara, T.; Sieber, S.; Morokuma, K. *J. Phys. Chem.* **1996**, *100*, 19357–19363.
- (29) Bearpark, M. J.; Larkin, S. M.; Vreven, T. *J. Phys. Chem. A* **2008**, *112*, 7286–7295.
- (30) Fingerhut, B. P.; Oesterling, S.; Haiser, K.; Heil, K.; Glas, A.; Schreier, W. J.; Zinth, W.; Carell, T.; de Vivie-Riedle, R. *J. Chem. Phys.* **2012**, *136*, 204307.
- (31) Werner, H.-J.; Knowles, P. J.; Knizia, G.; Manby, F. R.; Schütz, M.; Celani, P.; Korona, T.; Lindh, R.; Mitrushenkov, A.; Rauhut, G.; Shamasundar, K. R.; Adler, T. B.; Amos, R. D.; Bernhardsson, A.; Berning, A.; Cooper, D. L.; Deegan, M. J. O.; Dobbyn, A. J.; Eckert, F.; Goll, E.; Hampel, C.; Hesselmann, A.; Hetzer, G.; Hrenar, T.; Jansen, G.; Köppl, C.; Liu, Y.; Lloyd, A. W.; Mata, R. A.; May, A. J.; McNicholas, S. J.; Meyer, W.; Mura, M. E.; Nicklass, A.; O'Neill, D. P.; Palmieri, P.; Peng, D.; Pflüger, K.; Pitzer, R.; Reiher, M.; Shiozaki, T.; Stoll, H.; Stone, A. J.; Tarroni, R.; Thorsteinsson, T.; Wang, M. *MOLPRO*, version 2012.1, 2012.
- (32) Tal-Ezer, H.; Kosloff, R. *J. Chem. Phys.* **1984**, *81*, 3967–3971.
- (33) Wilson, E. B., Jr.; Decius, J. C.; Cross, P. C. *Molecular Vibrations*; McGraw-Hill: New York, USA, 1955.
- (34) Schaad, L.; Hu, J. J. *Mol. Struct.: THEOCHEM* **1989**, *185*, 203–215.
- (35) Kowalewski, M.; Mikosch, J.; Wester, R.; de Vivie-Riedle, R. *J. Phys. Chem. A* **2014**, *118*, 4661–4669.
- (36) Thallmair, S.; Fingerhut, B. P.; de Vivie-Riedle, R. *J. Phys. Chem. A* **2013**, *117*, 10626–10633.
- (37) Ammer, J.; Mayr, H. *J. Phys. Org. Chem.* **2013**, *26*, 956–969.
- (38) Ammer, J.; Sailer, C. F.; Riedle, E.; Mayr, H. *J. Am. Chem. Soc.* **2012**, *134*, 11481–11494.